Nonlinear low-to-high-frequency energy cascades in diatomic granular crystals

E. Kim,[1] R. Chaunsali,[1] H. Xu,[2] J. Jaworski,[1] J. Yang,[1,*] P. G. Kevrekidis,[2,3] and A. F. Vakakis[4]

[1]*Aeronautics and Astronautics, University of Washington, Seattle, Washington 98195-2400, USA*
[2]*Department of Mathematics and Statistics, University of Massachusetts, Amherst, Massachusetts 01003-4515, USA*
[3]*Center for Nonlinear Studies and Theoretical Division, Los Alamos National Laboratory, Los Alamos, New Mexico 87544, USA*
[4]*Department of Mechanical Science and Engineering, University of Illinois at Urbana Champaign, Urbana, Illinois 61822, USA*

We study wave propagation in strongly nonlinear one-dimensional diatomic granular crystals under an impact load. Depending on the mass ratio of the "light" to "heavy" beads, this system exhibits rich wave dynamics from highly localized traveling waves to highly dispersive waves featuring strong attenuation. We demonstrate experimentally the nonlinear resonant and antiresonant interactions of particles, and we verify that the nonlinear resonance results in strong wave attenuation, leading to highly efficient nonlinear energy cascading without relying on material damping. In this process, mechanical energy is transferred from low to high frequencies, while propagating waves emerge in both ordered and chaotic waveforms via a distinctive spatial cascading. This energy transfer mechanism from lower to higher frequencies and wave numbers is of particular significance toward the design of novel nonlinear acoustic metamaterials with inherently passive energy redistribution properties.

I. INTRODUCTION

Granular crystals, i.e., periodically packed arrays of solid particles interacting elastically via nonlinear contacts, have recently become popular test beds for understanding fundamental structures emerging within nonlinear wave dynamics, such as traveling waves [1–4], shock waves [5–7], discrete breathers [8,9], and nanoptera [10]. In these systems, tunable energy transport is of particular interest. For example, the wave propagation speed can vary significantly from linear to highly nonlinear regimes by changing the external compression applied to the granular system [1]. The energy propagation patterns can be tuned from highly localized to modulated or widely dispersed shapes by introducing local resonances in constituents [10]. The controllable degree of disorder also changes the nature of energy attenuation (as has been shown, e.g., in settings of decorated chains [11] or strong inertial mismatches [12]), enabling both exponential and power-law type scenarios [13,14]. This wealth of energy transport characteristics stems from the widely tunable interplay of nonlinearity, discreteness, and heterogeneity in such media.

Among the different heterogeneous variants of granular crystals, an ordered diatomic granular crystal—in the form of alternating heavy and light particles—is one of the most prototypical ones [3,15,16]. Remarkably, this simple *dimer* lattice shows highly intriguing energy transport phenomena. Previous studies demonstrated that diatomic granular chains may support various types of highly localized traveling waves, nonlinear beating pulses, and highly dispersive waves, depending on the mass ratio of the heavy and light beads [3,15–17]. It is of particular interest that wave attenuation can be maximized at a countably infinite number of mass ratios, while efficient transmission of energy without attenuation can also occur at another set of a countably infinite number of mass ratios, resulting in highly nonlinear solitary traveling

waves. This pertains to the so-called nonlinear *resonance* and *antiresonance* mechanisms [3,16]. These mechanisms can be intuitively understood when one considers the traveling-wave front and its immediate wave tail as *driving* and *driven* systems, respectively. The mass ratios satisfying the resonance and antiresonance conditions appear in an interlaced manner as the relevant parameter is varied. Despite previous theoretical and numerical studies on these resonance and antiresonance mechanisms, corresponding experimental work has been extremely limited [18].

Here, we advance considerably the experimental state of the art of the system by enabling a full-field visualization of the lattice's dynamics via laser Doppler vibrometry. These experimental advances, in turn, lead us to consider crucial theoretical and numerical aspects, such as the nonlinear energy transfer mechanisms across length and time scales. Specifically, we investigate how the resonances chiefly disintegrate and transfer energy into stable periodic modes, leading to extremely efficient nonlinear energy scattering and impact mitigation mechanisms. The remainder of the energy is partitioned to a wide range of frequencies and modes, resulting in an apparently chaotic spatial tail dynamics. This set of features is in sharp contradistinction with the antiresonance scenario where the energy appears to localize in traveling-wave *quanta* (i.e., isolated wave packets).

Our approach toward exploring the energy transfer mechanisms in granular crystals, in addition to substantial experimental developments, is motivated theoretically by the usefulness of this type of approach in revealing cascading dynamics in a large variety of other systems. These include classical and quantum fluids [19,20], plasmas [21], and solid structures such as vibrating thin plates [22–24]. Previous studies tackled the topic of energy distribution in granular crystals in the context of tapered and decorated chains [2,4,5], disordered settings [6], chains bearing impurities [25], interaction of waves with their own radiation [26], and that of narrow or broadband frequency signals with waves stemming from reflections [27]. Nevertheless, the mechanism of energy cascading across time and length scales has not been suitably

_____

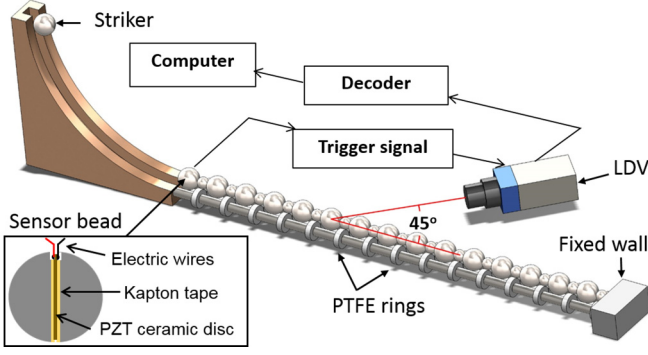*Author to whom all correspondence should be addressed: jkyang@aa.washington.edu

FIG. 1. (Color online) Schematic of the experimental setup for measuring nonlinear wave propagation in a diatomic granular crystal. The inset shows a cross section of the sensor particle.

explored yet. We believe that this study will plant the seeds for future investigations of such energy cascading dynamics in granular crystals as well as nonlinear lattice systems more generally.

II. EXPERIMENTAL AND NUMERICAL SETUP

Figure 1 shows the test setup consisting of a granular chain, a striker, and a laser Doppler vibrometer (LDV). The chain is composed of alternating "heavy" and "light" spherical particles (see Table I for the specific numbers of the heavy and light particles). All particles are made of chrome steel ($E = 210$ GPa, $v = 0.29$, $\rho = 7810$ kg/m^3). The radius of the heavy particles is $R = 9.525$ mm. We alter the radius of the light particles to set various mass ratios for the chain (Table I). We position the smaller particles on polytetrafluoroethylene (PTFE) rings tied to stainless steel rods to align the center of mass of all particles (Fig. 1). We generate nonlinear stress waves in the granular crystal by impacting one end of the chain with a striker, which is identical to the heavy particle. The striker is released from a ramp and attains an impact velocity of 0.94 ± 0.017 m/s, hitting the first bead, which is a heavy bead with an embedded piezoelectric ceramic disk at its center (see the inset of Fig. 1). At the time of impact, this sensor bead generates high voltage, which triggers our data acquisition system. The other end of the chain is fixed with a heavy steel wall.

We position the LDV at a slanted angle (45° in this study) to measure the velocity of a particle in each impact event (Fig. 1). We repeatedly measure the particle's velocity by shifting the LDV along the guiding rail and synchronize the measured data with respect to the striker's impact moment to reconstruct the wave-propagation profiles. We examine the

propagation of waves in two antiresonance cases, labeled AR1 (the homogeneous case, operating as a benchmark) and AR2, and in two resonance cases, labeled R1 and R2 [3,16]. Details of the dimensions and mass ratio of each model are summarized in Table I.

We complement these experimental results by numerical simulations with a discrete element model. The chain is modeled with point masses, which are connected by nonlinear springs representing the Hertzian contact between spheres [28]. The contact force between the nth and the $(n+1)$th bead is defined in terms of the relative displacement as follows:

$$F = \beta[u_n - u_{n+1}]_+^{3/2},$$

where β is a contact coefficient that depends on the material properties and geometry of the two objects in contact. In the case of a contact between large and small beads made of an identical material, the coefficient is defined as follows:

$$\beta = \frac{2E}{3(1-v^2)}\sqrt{\frac{R_L R_S}{R_L + R_S}},$$

where E and v are Young's modulus and Poisson's ratio of the beads, respectively, and R_L and R_S are the radius of the large and small beads, respectively [28].

Therefore, the equations of motion of the diatomic granular chain can be written as follows:

$$M_{2n-1}\ddot{u}_{2n-1} = \beta[u_{2n-2} - u_{2n-1}]_+^{3/2} - \beta[u_{2n-1} - u_{2n}]_+^{3/2},$$
$$M_{2n}\ddot{u}_{2n} = \beta[u_{2n-1} - u_{2n}]_+^{3/2} - \beta[u_{2n} - u_{2n+1}]_+^{3/2}.$$

Here M and u represent the mass and displacement of particles (odd and even subscripts correspond to heavy and light beads), β is the contact coefficient between two particles, and $[s]_+ = \max(s,0)$, implying that the system does not support tensile force. We note that the dynamics of this system is fully rescalable with energy, so for sufficiently small impulsive excitations the results do not change qualitatively [3,16].

The equations of motion of the granular chain are solved numerically using the Runge-Kutta method with a 10^{-7} s time step. For this numerical simulation, we use a 300-particle chain—although only a fraction of these, typically 150, are shown in simulations, e.g., Fig. 2. The numerical simulation shows an accuracy of about 0.004% error in terms of the total energy conserved during a 20 ms period. It should be noted that we neglect material damping in the numerical simulation in order to focus on the wave attenuation caused solely by energy redistribution in the chain.

TABLE I. Mass ratio and chain length of each experiment model.

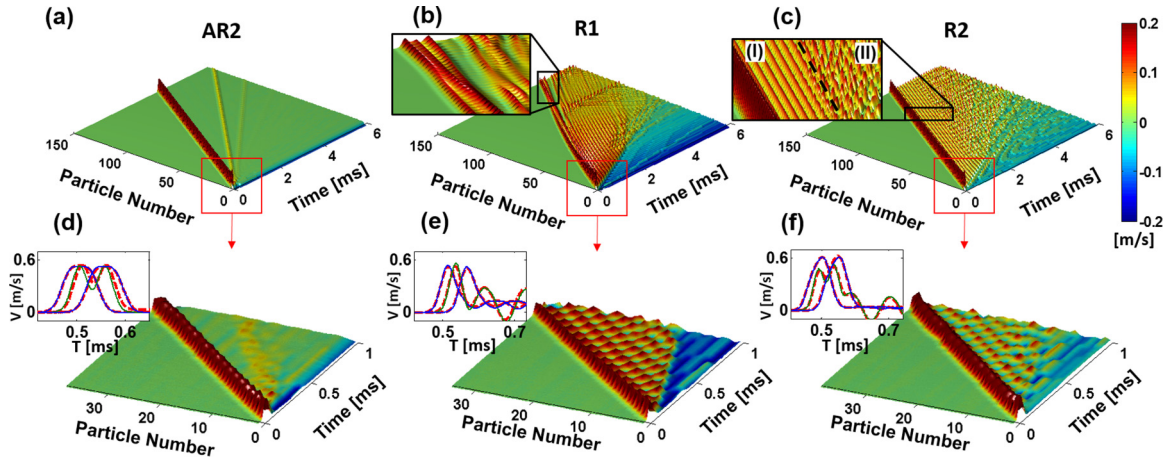| Model ID	Large bead diameter [mm]	Small bead diameter [mm]	Mass ratio	Chain length [mm] (number of beads)
AR1	19.050	19.050	1	609.6 (32)
R1	19.050	15.978	0.59	595.5 (34)
AR2	19.050	13.333	0.34	615.3 (38)
R2	19.050	11.839	0.24	605.9 (39)

FIG. 2. (Color online) Numerical and experimental surface maps for (a),(d) AR2, (b),(e) R1, and (c),(f) R2. The insets in (b) and (c) show an enlarged view of the nonlinear wave beating phenomenon in R1, and regular (I) and irregular (II) forms of the wave tail in R2, respectively. The insets in (d)–(f) illustrate comparisons of three successive (heavy-light-heavy) particles' velocity profiles between numerical [solid blue (heavy) and green (light)] and experimental (dashed red) results.

III. RESULTS AND DISCUSSION

Figure 2 shows numerical and experimental surface maps of the wave propagation in AR2, R1, and R2. In Fig. 2(a), the impact leads to the formation of a number of robust solitary pulses (three of these pulses are directly visible), which *quantize* the energy repartitioning it primarily into the first one [29,30]. The experimental results in Fig. 2(d) obtained by the LDV corroborate the numerical simulations, though the tertiary packet is not distinguishable due to the dissipation in experiments. It should also be noted that Figs. 2(a) and 2(d) employ different time and length scales because of the shorter granular chain used in experiments. In this antiresonance case, the traveling waves propagate with almost constant speeds without shedding energy behind the leading pulses. The velocities of these wave packets follow the relationship, $V \sim F_m^{1/6}$, where F_m is the peak amplitude of the dynamic force. This is the same as the conventional solitary wave in a homogeneous chain (i.e., AR1), which shows a single hump with its wavelength having a diameter of approximately five particles [1]. In AR2, the wavelength is wider than that in AR1 (see Appendix 1), and the heavy and light particles exhibit different velocity profiles [3]. We verified experimentally the waveform in AR2 as shown in the inset of Fig. 2(d).

In sharp contrast to antiresonances, resonances cause the propagating wave to shed its energy behind in the form of oscillating tails, thereby attenuating the leading pulses [see Figs. 2(b) and 2(c) for R1 and R2, respectively] [16]. We accurately measured the particle velocity profiles in these cases as well [see Figs. 2(e) and 2(f)]. In R1, the primary wave loses a considerable fraction of its energy by forming a wave tail oscillating initially in a regular fashion. However, after approximately 80 particles, three leading peaks form a wave packet [see the inset in Fig. 2(b)]. These pulses exchange energy among them as the wave packet propagates in the medium. This behavior is attributed to the so-called nonlinear beating phenomenon [16]. We observe that once the nonlinear beating starts, the energy transfer from the leading wave packet to the wave tail is substantially reduced, as the

relevant waveform *detaches* itself from the rest of the radiative tail. In R2, however, the primary wave continuously loses its energy to the wave tail. In this case, as well as in that of higher-order resonances, the oscillations of the wave tail retain a very regular structure just behind the primary wave. They eventually transform to apparently chaotic forms within the far-field [see regions (I) and (II) in the inset in Fig. 2(c)].

To further investigate the energy dispersion mechanism, we consider the relevant phenomenology in the Fourier domain. Figure 3(a) shows the frequency spectrum of the particles' velocity profiles in AR2, where the majority of energy is concentrated in low frequencies. In R1 [Fig. 3(b)], however, we find that a strong high-frequency signal (∼9 kHz) appears, and the magnitude of the low-frequency signal decreases during the primary pulse's shedding its energy to the wave tail (around up to 80 beads). This predominant mechanism of energy transfer ceases to exist as soon as the nonlinear beating starts. This represents the fact that the mechanical energy carried initially by the low-frequency primary pulse is redistributed to the higher-frequency contained in the wave tail due to the nonlinear resonance mechanism, but it is subsequently trapped in the beating mechanism without further substantial decay. In R2, this energy transfer from low to high frequencies happens persistently [see Fig. 3(c)] due to the continuous energy shedding to the wave tail. We can discern in the relevant frequency patterns the presence of regular oscillations in the wave tail [corresponding to part (I) in the inset of Fig. 2(c)]. Additionally, there exists a fraction of the energy deposited to a wide range of frequencies corresponding to a dispersion of the energy in other modes, resulting in the apparently chaotic oscillations of region (II) within the inset of Fig. 2(c).

Equally telling as the frequency-domain responses are the wave-number plots in Figs. 3(d)–3(f). In contrast to AR2, the resonance cases reveal how the energy of the primary wave at small wave numbers is converted to a wave number around $\pi/2$ in the wave tail [see Figs. 3(e) and 3(f) in comparison to Fig. 3(d)]. Remarkably, this length scale corresponds to the length of two sets of heavy and light beads. We note that the two strong signals near $\pi/2$ in R2 are because of the Fourier
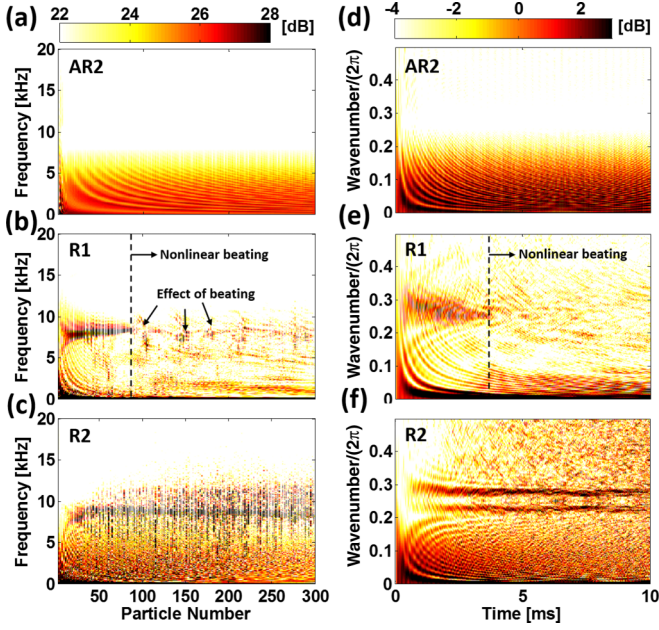
FIG. 3. (Color online) Frequency and wave-number spectra of particles' velocity profiles in (a),(d) AR2, (b),(e) R1, and (c),(f) R2, obtained from the analysis of the computational results and illustrating the presence of cascades associated with the redistribution of energy among different scales. The wave number is calculated based on the wavelength normalized by the average diameter of the large and small particles.
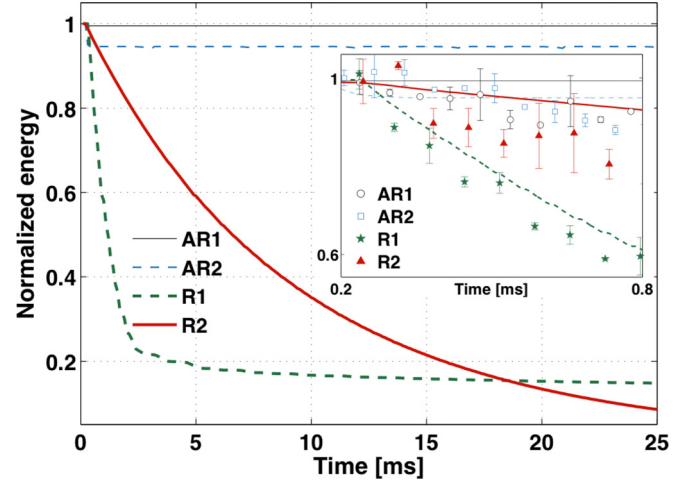

FIG. 4. (Color online) Normalized energy carried by the primary wave packet in antiresonances and resonances. The inset shows a comparison between the experimental and numerical results. The error bars represent standard deviations based on five tests.

transform of mixed signals from the heavy and light beads in an alternating pattern (Appendix 2). This wave-number trend suggests the emergence of a definitive *periodic traveling wave* pattern that is being excited in association with a periodicity of two beads. Such periodic patterns are witnessed experimentally in Figs. 2(e) and 2(f), and they have also been studied analytically in dimer chains [17]. Our wave-number analysis reveals the excitation of these states in a transient way for R1 until the beating pattern forms. In R2, contrarily, the pattern is persistent and clearly discernible in region (I) of Fig. 2(c), enabling the continuous transfer of energy from the principal wave to the associated background. Once again in R2, when the wave tail transforms to chaotic oscillations, the length scale also spreads out widely as denoted by the speckles in Fig. 3(f).

An alternative diagnostic toward the characterization of the energy transmission is provided in Fig. 4 under various antiresonance and resonance conditions. Here, we compare the energy carried by the leading wave packet after normalizing it with respect to the impact energy injected by the striker. Here is a brief description of how we quantify the energy. If we assume that the potential energy between the two particles in contact is equally distributed to the two particles, the total energy of the *n*th particle at time *t* can be defined as follows:

$$E_n(t) = \tfrac{1}{2}M_n\dot{u}_n^2 + \tfrac{1}{5}\beta[u_{n-1} - u_n]_+^{5/2} + \tfrac{1}{5}\beta[u_n - u_{n+1}]_+^{5/2}.$$

To calculate the energy of the leading wave, we conduct the summation of the energy for seven particles, which are wide enough to cover the envelope of the leading pulse in the AR1, AR2, and R2 cases. In R1, however, we add the energy of

nine particles to account for the total energy of the beating waveform. Again, the total energy of the leading waves is normalized with respect to the initial excitation energy, $E_0 = \tfrac{1}{2}M_0v_0^2$, where v_0 is the impact velocity of a striker.

In Fig. 4, we observe highly efficient and constant energy transmission in AR1 and AR2 due to the formation of solitary pulses. The normalized energy is less than 1 in AR2, which is caused by the trailing solitary waves generated in the transition region as explained above. In sharp contrast to such antiresonance cases, the primary pulse experiences a fast and dramatic attenuation in R1. About 80% of the energy is transferred to the wave tail within just 3 ms, which corresponds to the time the wave takes to propagate through the first 80 particles [see Fig. 2(b)]. Hence, the emerging periodic traveling wave is extremely efficient in rapidly draining the energy of the leading pulse. However, once the nonlinear beating pulse is formed, the transfer of energy to the wave tail is essentially suppressed. On the other hand, in R2, the reduction of normalized energy is slower compared to that in R1. Nonetheless, such wave attenuation happens continuously given the persistence in the latter case of the periodic traveling wave. As a result, the normalized energy carried by the primary pulse approaches zero asymptotically. This eventually leads the attenuation of the primary pulse in R2 to become larger than that in R1. Higher-order resonances share the principal characteristics of R2, as concerns the above phenomenology.

The distinctive energy scattering phenomena between R1 and R2 stem from the difference in the relative motions of the heavy and light beads. When the particles are squeezed by the leading wave, light particles move faster than heavy particles. The disparity between the heavy and light particles' motions becomes more evident as the mass ratio decreases. In R1, the light and heavy beads move at relatively similar frequencies due to the small difference in their masses (mass ratio of 0.59). This results in the fast energy scattering under the facilitated transition of energy between the heavy and light particles. In R2, however, the light particles' motions are much faster than those of heavy particles due to the small mass ratio

(only 0.24). This results in a slow—but more consistent—reduction of energy, leading to the higher wave attenuation performance than R1. Given the limited length of the granular crystal tested in this study, we obtained experimental data up to ~0.8 ms (inset of Fig. 4). We find that the experimental results corroborate the numerical simulations.

These observations provide us with a complete picture—in both real and Fourier space, in both time and frequency domains—of how wave attenuation mechanisms can be achieved on the basis of nonlinear resonance mechanisms. This type of process is fundamentally different from the conventional energy attenuation mechanisms relying on material damping and/or structural deformation effects. Here, the wave attenuation is achieved by maximizing the energy dispersion and redistribution within the chain of granular particles. The existence of damping in this system only enhances the wave attenuation. This is confirmed by our experimental data, where the energy of the primary pulse attenuates more than that in numerical simulations (Fig. 4). Moreover, the energy cascading from low to high frequency and large to small length scale plays a crucial role in a way that is partially reminiscent of similar cascading phenomena within fluidic systems.

IV. CONCLUSIONS

In the present work, we performed experimental and numerical investigations of the nonlinear resonance and antiresonance phenomena in ordered diatomic granular crystals and their connection to highly effective nonlinear frequency redistribution and cascading of energy across different scales. We verified the existence of efficient energy transfer mechanisms for resonances and robust traveling solitary waves for antiresonances. In particular, we demonstrated that the nonlinear resonance mechanism can be highly useful in attenuating impact energy by dispersing it to the wave tail. In this process, we found an interesting energy transition mechanism, i.e., the low-to-high-frequency energy transfer and large-to-small-scale energy cascading. This low-to-high-frequency energy transfer is a special one as it attains its maximum at nonlinear resonance condition. Moreover, the energy cascades are reminiscent of analogous cascades encountered in turbulent flows, which shows that acoustic metamaterials such as the granular diatomic chain considered herein can be tuned to possess this type of turbulence-like behavior. A dominant role within this mechanism was revealed to be played by periodic traveling waves, which appear to be excited either transiently (R1) or permanently (R2). This can offer a new way to designing nonlinear acoustic metamaterials based on inherently passive energy redistribution principles for impact mitigation purposes.

APPENDIX

1. Wavelength of the solitary waves in diatomic granular crystals

In this Appendix, we compare the wavelength of the solitary waves in diatomic granular chains at various mass ratios. We obtain the wavelength values from three different approaches: (i) the analytical method by Porter *et al.* [15] (solid blue curve); (ii) the numerical simulations via a discrete element method (green squares); and (iii) the experimental results via laser Doppler vibrometry (red circles) as shown in Fig. 5. In the numerical simulation and experiments, we count the number of particles (n) having a velocity larger than a threshold value in a fixed time frame, and we determine $n + 1$ as the wavelength considering the smoothly decreasing wave edges. Here, the threshold is set to be 0.1% of the maximum particle's velocity. It should be noted that the wavelength varies depending on the measurement moment due to the discreteness of the system, and it can be overestimated at a small threshold value. Therefore, we process multiple data points at various time frames for statistical analysis. In the analytic expression, the diameter of the wavelength is about five particles at a mass ratio 1, and it gradually increases and approaches approximately ten particle as the mass ratio approaches zero. In the experimental and numerical results, the diameter of the wavelength in AR1 is slightly larger than five particles. It is generally known that the diameter of the wavelength of the conventional solitary wave (in AR1) is about five particles. However, it has also been reported that the diameter of the wavelength in AR1 is close to seven particles if we account for extremely small wave
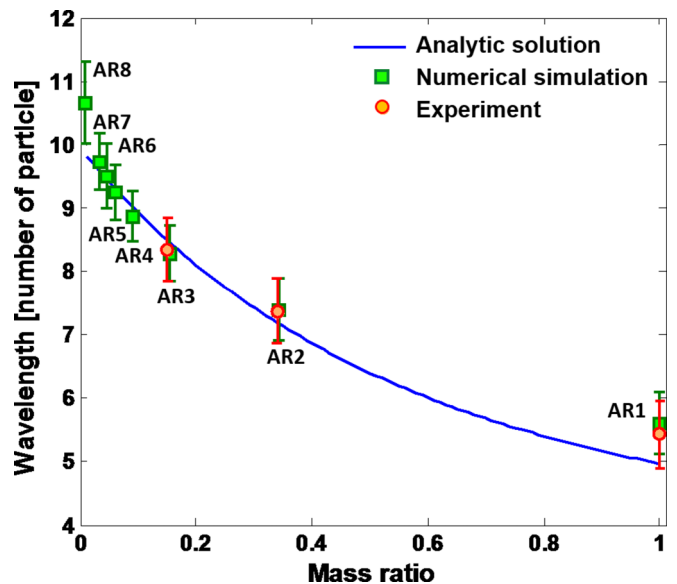

FIG. 5. (Color online) Wavelength of the solitary waves in a diatomic chain at various mass ratios from AR1 to AR8. The solid curve represents the analytical prediction based on Porter *et al.* [15]. Green squares and red circles are from numerical simulations and experiments, respectively.
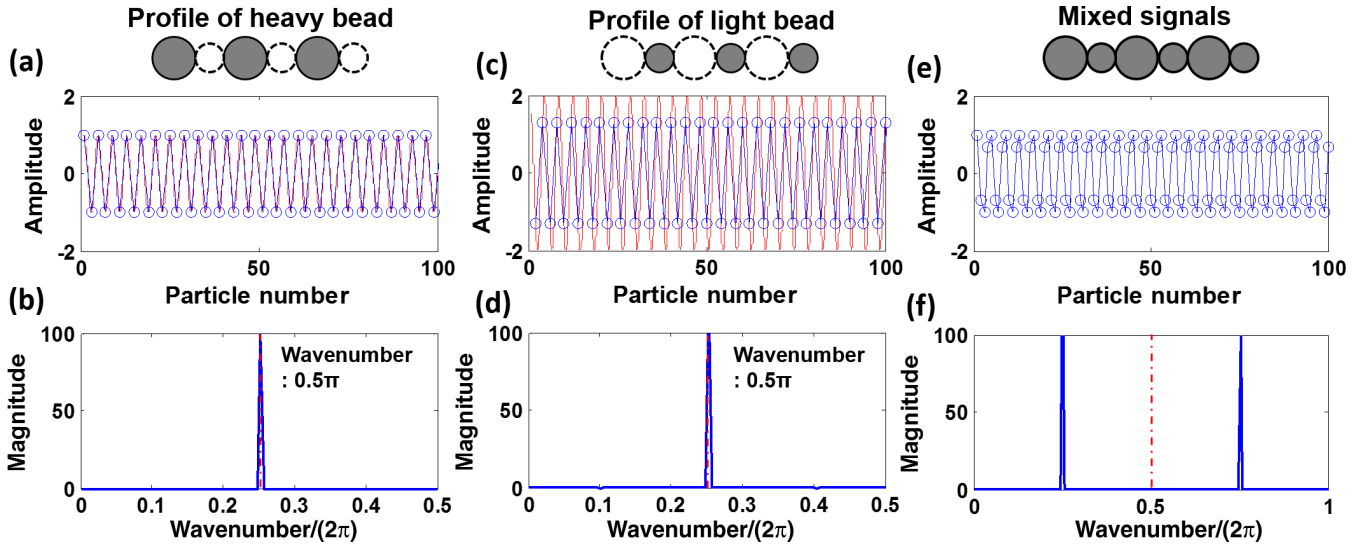
FIG. 6. (Color online) Wave-number analysis in the case in which two different profiles with an identical wave number of $\pi/2$ are mixed together in an alternating way. Based on the FFT analysis, (b), (d), and (f) show the wave number of the wave profiles in spatial domains for (a) heavy beads, (c) light beads, and (e) the mixed data of the two, respectively. In (a) and (c), red curves represent continuous signals, while blue circles denote the sampled data at particle positions.

edges [2]. This can be captured when we lower the threshold value of the detectable wave velocity significantly.

2. Wave number of velocity profiles in the first (R1) and second (R2) resonances

The high wave-number components in the nonlinear resonance R1 and R2, shown in Figs. 3(e) and 3(f), respectively, correspond to the *regular* wave tail discussed in Figs. 2(b) and 2(c), where "heavy" and "light" beads oscillate in an ordered fashion in the near field of the primary pulse. When we perform fast Fourier transformation (FFT) of velocity profiles

of all beads (i.e., both heavy and light ones) in the spatial domain, we observe one or more wave numbers symmetric with respect to $\pi/2$, which corresponds to the wavelength identical to the four-particle distance. Here, in the calculation of the wave number, we use the number of particles instead of their actual dimensions for the sake of simplicity. The symmetry with respect to $\pi/2$ is due to the FFT of a mixed signal composed of two different velocity profiles. For example, the heavy particles show small-amplitude oscillations, while the light particles show larger-amplitude oscillations due to the smaller inertia. If we separate the signals into two profiles, namely "heavy" particle velocity profile and "light" particle
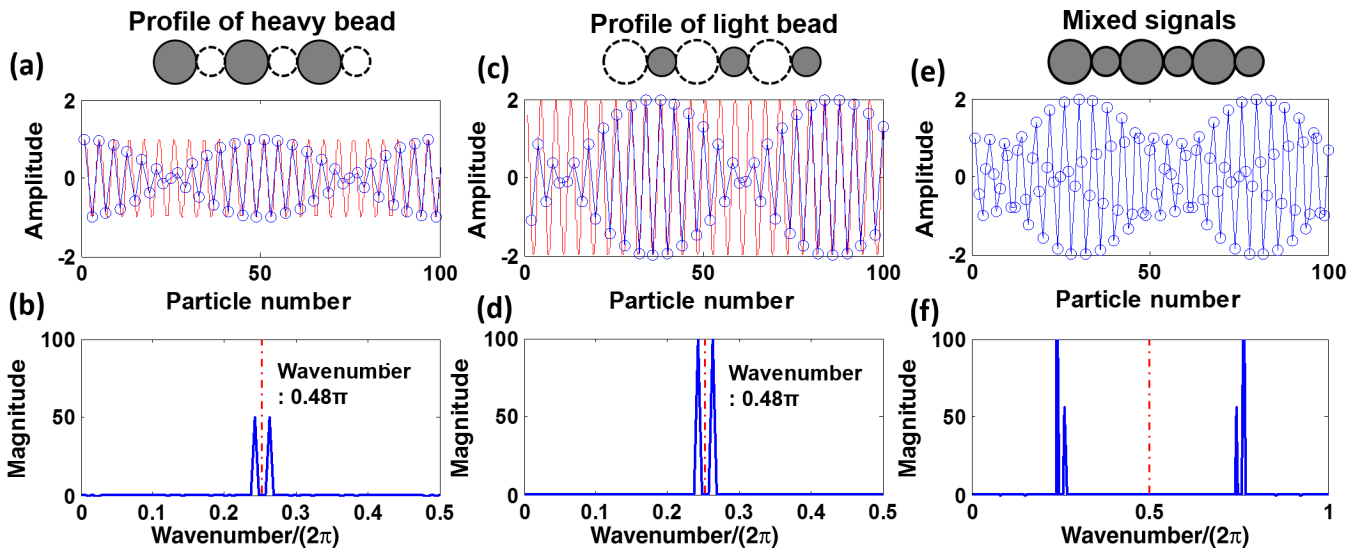

FIG. 7. (Color online) Wave-number analysis in the case in which two different profiles with an identical wave number of 0.48π are mixed together in an alternating way. Based on the FFT analysis, (b), (d), and (f) show the wave number of the wave profiles in spatial domains for (a) heavy beads, (c) light beads, and (e) the mixed data of the two, respectively. In (a) and (c), red curves represent continuous signals, while blue circles denote the sampled data at particle positions.

velocity profile [see Figs. 6(a) and 6(c)], the FFT of these signals shows wave numbers up to π, because the lattice constant is two particles in this case [see Figs. 6(b) and 6(d)]. These signals are symmetric with respect to the central wave number $\pi/2$ [see Figs. 6(b) and 6(d)] due to the nature of the FFT of real-valued signals. This is also referred to as a spatial aliasing effect. It should be noted that one is a mirrored image of the other. Therefore, if the wave number of the harmonic signal is $\pi/2$, we can only see a single peak at $\pi/2$ [Figs. 6(b) and 6(d)]. Otherwise, the FFT shows two peaks in symmetry with respect to $\pi/2$ [Figs. 7(b) and 7(d)].

In the original signals where the two velocity profiles are mixed in an alternating pattern, the lattice constant is a single particle. Therefore, the FFT of this signal shows wave numbers up to 2π, and it is symmetric with respect to π. Interestingly, in this FFT signal of the combined data, the symmetric wave numbers in the separated velocity profiles (in the range of 0 to π) appear on top of each other in the same wave-number range, from 0 to π. Therefore, when the oscillations of both "heavy" and "light" particles have a single wave number of $\pi/2$, only one wave number ($\pi/2$) appears in the FFT of the combined signal within the range from 0 to π. On the other hand, when they have the same wave number that is other than $\pi/2$, double peaks symmetric with respect to $\pi/2$ appear. If the two signals have different wave numbers, the FFT signals show four peaks in symmetry with respect to $\pi/2$.

In the first resonance (R1), the high wave-number component is initially dispersed, and then it is focused around $\pi/2$ as the wave propagates up to about 80 particles. In the second resonance R2, however, two distinctive lines continuously appear as the wave propagates, which represent that the wave numbers of the heavy and light particle oscillations are similar to each other with a minor offset from the $\pi/2$. Again, this difference between R1 and R2 stems from the difference of the relative particles' motions, as we explained in Sec. III.

[1] V. F. Nesterenko, *Dynamics of Heterogeneous Materials* (Springer-Verlag, New York, 2001), Chap. 1.

[2] S. Sen, J. Hong, J. Bang, E. Avalos, and R. Doney, Phys. Rep. **462**, 21 (2008).

[3] K. R. Jayaprakash, Y. Starosvetsky, and A. F. Vakakis, Phys. Rev. E **83**, 036606 (2011).

[4] U. Harbola, A. Rosas, A. H. Romero, and K. Lindenberg, Phys. Rev. E **82**, 011306 (2010).

[5] R. Doney and S. Sen, Phys. Rev. Lett. **97**, 155502 (2006).

[6] J. Hong, Phys. Rev. Lett. **94**, 108001 (2005).

[7] C. Daraio, V. F. Nesterenko, E. B. Herbold, and S. Jin, Phys. Rev. Lett. **96**, 058002 (2006).

[8] N. Boechler, G. Theocharis, S. Job, P. G. Kevrekidis, M. A. Porter, and C. Daraio, Phys. Rev. Lett. **104**, 244302 (2010).

[9] C. Chong, F. Li, J. Yang, M. O. Williams, I. G. Kevrekidis, P. G. Kevrekidis, and C. Daraio, Phys. Rev. E **89**, 032924 (2014).

[10] E. Kim, F. Li, C. Chong, G. Theocharis, J. Yang, and P. G. Kevrekidis, Phys. Rev. Lett. **114**, 118002 (2015).

[11] U. Harbola, A. Rosas, A. H. Romero, M. Esposito, and K. Lindenberg, Phys. Rev. E **80**, 051302 (2009).

[12] A. Breindel, D. Sun, and S. Sen, Appl. Phys. Lett. **99**, 063510 (2011).

[13] L. Ponson, N. Boechler, Y. M. Lai, M. A. Porter, P. G. Kevrekidis, and C. Daraio, Phys. Rev. E **82**, 021301 (2010).

[14] N. Upadhyaya, L. R. Gomez, and V. Vitelli, Phys. Rev. X **4**, 011045 (2014).

[15] M. A. Porter, C. Daraio, E. B. Herbold, I. Szelengowicz, and P. G. Kevrekidis, Phys. Rev. E **77**, 015601(R) (2008); M. A. Porter, C. Daraio, I. Szelengowicz, E. B. Herbold, and P. G. Kevrekidis, Physica D **238**, 666 (2009).

[16] K. R. Jayaprakash, Y. Starosvetsky, A. F. Vakakis, and O. V. Gendelman, J. Nonlin. Sci. **23**, 363 (2013).

[17] M. Betti and D. E. Pelinovsky, J. Nonlin. Sci. **23**, 689 (2013).

[18] R. Potekin, K. R. Jayaprakash, D. M. MacFarland, K. Remick, L. A. Bergman, and A. F. Vakakis, Exp. Mech. **53**, 861 (2013).

[19] P. Holmes, J. L. Lumley, G. Berkooz, and C. W. Rowley, *Turbulence, Coherent Structures, Dynamical Systems and Symmetry* (Cambridge University Press, Cambridge, 2012).

[20] S. V. Nazarenko, *Wave Turbulence*, Lecture Notes in Physics Vol. 825 (Springer, Heidelberg, 2011).

[21] A. A. Vedenov, in *Reviews of Plasma Physics*, edited by M. A. Leontovich (Consultants Bureau, New York, 1967), Vol. 3

[22] G. During, C. Josserand, and S. Rica, Phys. Rev. Lett. **97**, 025503 (2006).

[23] A. Boudaoud, O. Cadot, B. Odille, and C. Touze, Phys. Rev. Lett. **100**, 234504 (2008).

[24] N. Mordant, Phys. Rev. Lett. **100**, 234505 (2008).

[25] S. Job, F. Santibanez, F. Tapia, and F. Melo, Phys. Rev. E **80**, 025602(R) (2009).

[26] Y. Takato and S. Sen, Europhys. Lett. **100**, 24003 (2012).

[27] D. A. Hutchins, J. Yang, O. Akanji, O. J. Thomas, L. A. J. Davies, S. Freear, S. Harput, N. Saffari, and P. Gelat, Europhys. Lett. **109**, 54002 (2015).

[28] K. L. Johnson, *Contact Mechanics* (Cambridge University Press, Cambridge, 1985).

[29] S. Job, F. Melo, A. Sokolow, and S. Sen, Granular Matter **10**, 13 (2007).

[30] A. Sokolow, E. G. Bittle, and S. Sen, Europhys. Lett. **77**, 24002 (2007).